

Resilient Operation of Grid-Forming Inverters under Large-scale Disturbances in Low Inertia Power System

Muhammad F. Umar^{1,2}, (Member, IEEE), Amirhosein Gohari Nazari¹, (Student Member, IEEE), Mohammad B. Shadmand¹, (Senior Member, IEEE), and Haitham Abu-Rub³ (Fellow, IEEE)

¹Department of Electrical and Computer Engineering, University of Illinois Chicago, Chicago, IL, USA

Corresponding author: Mohammad B. Shadmand (e-mail: shadmand@uic.edu).

This work was supported in part by the U.S. National Science Foundation under Grant ECCS-211444 and Grant NPRP12C-0814-190012 and Grant NPRP12C-33905-SP-220 from the Qatar National Research Fund (a member of Qatar Foundation). The statements made herein are solely the responsibility of the author.

ABSTRACT The future power grid is transitioning towards a low inertia power system due to the displacement of synchronous generators (SG) based generation sources and incorporating inverters based renewable energy resources. Heterogeneous grid-forming inverters (GFMIs) are expected to be dominant sources in the power generation mix due to several benefits that are inherited in this inverter control. However, these GFMIs impose different transients on the power grid that did not exist in the conventional power grid. The effect of this heterogeneity on the dynamic behavior of such power grid with a fleet of GFMIs becomes more significant under large scale disturbances such as short circuit faults. Particularly, because of the non-coherent and heterogeneous dynamic behavior of GFMIs in presence of the conventional overcurrent protection schemes, several challenges are posed on the resiliency of a power grid during a fault and in post-fault state. To improve the resiliency of power grid with heterogeneous GFMIs during these conditions, a coherency enforcement scheme among heterogeneous GFMI is proposed. This ensures a coherent transition of GFMIs from the normal to fault ride-through mode and from the fault-ride through mode to normal condition when fault is cleared. Moreover, the proposed improvements in GFMI control prevents the excessive change/acceleration in the voltage angle of GFMIs that prevents the loss of synchronism, improves the dynamic behavior of GFMIs and ensure seamless operation under large-scale disturbances, resultantly, enhances resiliency of power grid. These claims in the resiliency enhancements for a power grid dominated with heterogeneous GFMIs under largescale disturbances are validated via hardware-in-the-loop (HIL) experimental case studies.

INDEX TERMS coherent transient response, fault-ride through, grid forming inverters, coherency enforcement, low inertia power system.

I. INTRODUCTION

Increased generation from renewable energy sources comprised of solar, wind, etc. has led to a transition of the existing power system to highly distributed generation (DG) rather than centralized. Mostly, power electronics converters are required to integrate these propagating DG sources with the power grid [1]. This approach will move the future power grid to a new energy paradigm, known as a power electronics-dominated grid (PEDG) [2]. Due to dominant inverter based generation and retiring of several synchronous generators (SGs), PEDG is an intrinsically low inertia power system [2]. Conventionally, the DGs are controlled in grid-following (GFLIs) mode of operation to feed power into the grid according to commanded setpoints. However, due to voltage and frequency instability issues during the weak grid conditions and challenges in the island operation of a

microgrid comprised of GFLIs [3], another popular control approach for inverters is grid forming control [4].

Primarily, the grid-forming inverters (GFMIs) regulate the frequency and voltage of a grid cluster to ensure stable operation. Various control strategies for GFMIs are proposed in the literature, including droop control [5], virtual synchronous generator-based control [6], virtual oscillator control [7], power synchronization control [8], etc. PEDG comprised of GFMIs provides added advantages and auxiliary services such as virtual inertia emulation, voltage, and frequency support, grid-tied and island operation, etc. Therefore, this makes GFMIs an attractive option to replace the synchronous generators (SG) in the futuristic power grids.

However, in practical applications the GFMIs installed at various locations in the power grid are from different manufacturers and might have different power ratings, diverse

1

²Department of Electrical and Computer Engineering, Texas A&M University at Qatar, Doha, Qatar

³College of Science and Engineering, Hamad Bin Khalifa University, Doha, Qatar



controllers, and controllers' settings. This brings an intrinsic heterogeneity in the dynamic response of GFMIs.

The operational challenge associated with heterogeneous GFMIs is non-coherent/ dissimilar dynamic characteristics during disturbances. These non-coherent dynamics can be even more problematic during large-scale disturbances which can impact the stability of the low-inertia PEDG. Specifically, when a short-circuit fault occurs in PEDG, the conventional overcurrent protection schemes are triggered to prevent high magnitude fault current flowing from GFMIs and results in significant drop in the grid voltage. Due to which the active power supplied by the GFMI decreases drastically. This will cause the effective voltage angles of heterogeneous GFMI to accelerate to match the reference active power. Nevertheless, due to the heterogeneity, each GFMI will exhibit different dynamic response under this disturbance, consequently, this may deviate these voltage angles away from the initial synchronized operation [9]. Furthermore, if this acceleration of voltage angles of GFMIs continues, it can make the voltage angles surpass the critical angle (is maximum value of voltage angle under which system remain stable during a fault and the equal area criterion is satisfied) and that lead to potential transient instability [10]. Another challenge is the transition from fault to normal operation, as during the fault when output current of GFMIs is limited, the inner controller becomes saturated and in transition from fault to normal conditions this can produce huge oscillations in the output current and voltage of GFMIs. Thus, effective coordination within the restoration mechanism is critical for seamless transition and resilient operation of those inverters.

In a conventional power system that is dominated by SG based generation, a coherency-based grouping/rescheduling of SGs is performed to dampen the inter-area oscillations and prevent transient instability under large-scale disturbances [11, 12]. Unlike the conventional power grid, which is dominated by high inertia SGs, the possibility of large acceleration in voltage angle during large-scale disturbances of GFMIs is enlarged due to the intrinsically lower inertia. Resultantly it can adversely impact resiliency of PEDG by causing oscillations in the output current and grid voltage. Another challenge is the variance of the output impedance of GFMIs during the faults [13]. Determining the value of the fault current becomes difficult and it is highly challenging to ensure resilient operation of such low inertia PEDG during the large-scale disturbances.

Various approaches are proposed in the existing literature to improve the operation of the GFMIs under the grid faults. Virtual impedance (VI)-based current limiting scheme is proposed in [14-16]. It relies on modifying the effective impedance of a GFMI to limit the output current to the defined nominal range and operate the GFMI during fault. Nevertheless, VI may excessively limit the current even during the very light overload condition under a disturbance, thus enforcing GFMI to operate in under-utilized mode. Another method for resilient operation of GFMI during faults is to switch control from grid-forming to grid-

following mode [17]. However, with this approach, all the GFMI's control features and benefits are lost. Furthermore, this scheme requires a backup PLL because, in weak grid conditions, the PLL loop suffers instability and will give erroneous output to the controller which may cause instability.

The overcurrent protection for GFMI can be embedded in the inner-loop controller. The works in [18, 19] proposed adding a saturation limit to the current reference in the inner current controller. However, the saturation based current limitation schemes suffers from instability during the transition from the fault to normal operation of GFMI. This instability is usually caused by the windup of the voltage controllers during the fault [20, 21]. Moreover, determining the accurate saturation limit according to the intensity of the fault and avoiding the windup of the voltage controller is still a big challenge. If the saturation limit is inappropriately devised, it can saturate the current limiters which can seriously affect the stability of the grid cluster [22]. Similarly, a switch-level current limiting is another method discussed in the literature. This method directly changes the modulation circuit to limit the overcurrent during a fault. In [23], a hysteresis loop is proposed to limit the overcurrent during a large-scale disturbance. In [24], an experimental implementation of the switch-level current limiting is demonstrated, however, bypassing/restricting the original switching signal from GFMI may lead to controller instability and causes degradation in the power quality.

Another solution discussed in literature to protect the GFMIs from overcurrent is to apply voltage limiter-based overcurrent protection. This scheme applies voltage limits on the voltage reference to minimize the difference between the terminal voltage and generated voltage reference [25]. In [26], a voltage limiting scheme is proposed that devises the voltage limits based on each phase current. However, this scheme introduces non-sinusoidal currents when the protection scheme is activated. Moreover, this type of direct voltage limiting requires an additional anti-windup control scheme to avoid stability issues when the fault is cleared, and system restored to normal conditions. The concept of resiliency [27] discussed in this work is to enable GFMIs with a seamless, stable and uninterrupted operation during large-scale disturbances such as short circuit faults and in post-disturbance scenarios. Thus, in Table I summarizes a comparative analysis between different schemes presented in existing literature for GFMI operation during a large-scale disturbance and the proposed coherency enforced approach. The resiliency performance of each scheme is analyzed based on overcurrent limiting performance, fault-ride through operation and system restoration in post-disturbance conditions.

The coherency enforcement control used in this work was initially developed by authors of this manuscript and more details about that work are available in [28-30]. The main focus of earlier work was related to achieving aggregated reference model development for a large-scale power system with a high number of DGs. The main difference between



Scheme	Overcurrent limitation performance	Fault-ride through operation	System restoration in post-disturbance
Virtual impedance [14- 16]	Capability to limit high fault current under severe faults.	Complex process to design parameters that introduce tradeoff between stability and fault current limiting ability.	Able to restore the system without additional controller action.
Switching to grid- following operation [17]	Ability to limit high fault currents effectively.	 Benefits of grid-forming controller are lost. Requires PLL to remain synchronize with AC grid that can pose instability issues during fault. 	Requires a separate control algorithm to switch back to GFMI operation.
Current limiting-based protection [18-22]	Controller may saturate in current limiting under severe faults.	Temporary overcurrent in fault-ride through operation.	 Suffers from transient instability under fault recovery period. Requires a separate anti-windup control for inner current loop.
Switch-level current limiter [23-24]	Can quickly limit high fault current.	 Can cause instability while blocking the switches. Degrades power quality because of waveform peak clipping. 	Requires additional anti-windup control loop to restore the normal operation.
Voltage based overcurrent limiting [25-26]	 High fault current limiting capability requires information on the network parameters. 	 Introduces non-sinusoidal phase current during fault. Temporary overcurrent in fault-ride through operation. 	Able to restore to normal conditions when disturbance is eliminated.
Proposed coherency enforcement-based approach	Capability to limit high fault current with high accuracy under severe disturbances.	No temporary overcurrent or oscillations in the phase current during the fault. Prevents the excessive acceleration of the voltage angles of GFMI during the fault and transient instability.	Seamless transition from fault to normal conditions when fault is cleared.

this work and the author's previous works is the application of a devised scheme for improving resiliency of a low inertia PEDG for large-scale disturbances such as, short circuit faults. Specifically, in this work the authors are leveraging the concept of enforcing coherency among heterogeneous GFMIs to improve the dynamic response of GFMIs in such a manner that helps to increase the resiliency of low inertia PEDG during fault and post-fault scenarios. Moreover, a fault-current limiting method is presented in this paper to ensure a coherent behavior of GFMI during transition from normal condition to fault-ride through the condition, which happens after a fault and during the transition from fault to normal condition. The previous studies on fault current limiting didn't ensure a coherent shift of GFMIs during the transient state from normal condition to fault ride-through condition, and the transient state happens after fault clears. Other than limiting the fault current, the coherent routine presented for fault detection ensures less frequency and active power isolation when GFMIs move to fault ride through regime or move from fault ride through to normal condition.

Thus, the main contributions of this work include,

- Preventing excessive acceleration of the voltage angle of heterogenous GFMI during a large-scale disturbance in low inertia power system. This allows to minimize the risk of transient instability and loss of synchronism among network of GFMIs in low inertia power system.
- Ability to effectively protect GFMIs via limiting the high amount of current within the bearable range of power electronics-based switches in GFMIs that enable an uninterruptible operation of GFMIs during largescale disturbances.

- Visualization of impact from different levels of heterogeneity in GFMIs via introducing coherency enforcement factor that helps to analyze the dynamic behavior of these heterogeneous GFMIs during largescale disturbances.
- Enhancing GFMI's overcurrent protection with a FDL module that compliments the coherency enforcement control and helps to prevent large oscillations in active power, reactive power, output current and frequency during a fault and in post-fault transition, thus, enabling a seamless operation during and in post large-scale disturbance.

The remainder of this paper is structured as follows: Section II explains the large-signal model GFMI and explores the cause of transient instability in GFMI under a large-scale disturbance. Section III presents the formulation of resiliency enhancement controller for GFMIs, and section IV presents the impact analysis of the proposed control scheme. Section V presents the case studies conducted by hardware-in-the-loop (HIL) experiments that are benchmarked with and without incorporating the proposed control modifications. Finally, the conclusion of the presented work is discussed in section VI.

II. LARGE-SIGANL MODELLING OF THE GFMI

Understanding the impacts from a large-scale disturbance, such as short-circuit fault, on the transient stability of a low inertia power systems/PEDG requires devising the large-signal model of GFMI. The primary controller of the GFMIs is based on the droop- control and the large-signal variation in the voltage angle and magnitude of the point of common coupling (PCC) voltage of GFMI is dictated by,



$$\delta_{gfmi} = \omega_0 t + d_p \int (P_{gmfi} - P_{set}) \tag{1}$$

$$v_p = V_{p0} + d_q (Q_{omfi} - Q_{set}) \tag{2}$$

where, ω_0 is the nominal frequency and δ_{gfmi} is the voltage angle of grid forming inverter. P_{gfmi} and P_{set} are the calculated and reference active power, respectively. The d_p and d_q are defined as the droop gains for the active and reactive power control loops. v_p and V_{p0} are the measured and nominal RMS voltage. Moreover, Q_{gfmi} and Q_{set} are the measured and reference reactive power. The active and reactive powers in stationary reference frame injected by GFMI are given as,

$$P_{gfmi} = 3 / 2(v_{p\alpha}i_{g\alpha} + v_{p\beta}i_{g\beta}) \tag{3}$$

$$Q_{gfmi} = 3/2(v_{p\beta}i_{g\alpha} - v_{pa}i_{g\beta}) \tag{4}$$

Moreover, the derivatives of output current of the GFMI in stationary reference frame is given by,

$$\frac{di_{g\alpha}}{dt} = \frac{1}{L_l} (v_{p\alpha} - R_l i_{g\alpha} - v_{ac\alpha})$$
 (5)

$$\frac{di_{g\beta}}{dt} = \frac{1}{L_l} (v_{p\beta} - R_l i_{g\beta} - v_{ac\beta})$$
 (6)

where $v_{pa}=V_{p0}sin(\omega t+\delta_{gfmi})$, $v_{p\beta}=-V_{p0}cos(\omega t+\delta_{gfmi})$, $v_{aca}=V_{ac}sin(\omega t)$, and $v_{ac\beta}=-V_{ac}cos(\omega t)$ are the PCC voltages of the GFMI and the common AC bus voltages in stationary reference frame, respectively. The derivative of the AC bus voltage in stationary reference frame is given by,

$$\frac{dv_{aca}}{dt} = \omega V_{ac} \cos \omega t = -\omega v_{ac\beta} \tag{7}$$

$$\frac{dv_{ac\beta}}{dt} = \omega V_{ac} \sin \omega t = \omega v_{ac\alpha}$$
 (8)

To capture the dynamics of the active and reactive power during the transient stage, the derivative of the (3) and (4) is calculated by applying chain rule and is given as,

$$\frac{dP_{gfmi}}{dt} = \frac{3}{2} \left(v_{p\alpha} \frac{di_{g\alpha}}{dt} + i_{g\alpha} \frac{dv_{p\alpha}}{dt} + v_{p\beta} \frac{di_{g\beta}}{dt} + i_{g\beta} \frac{dv_{p\beta}}{dt} \right)$$
(9)

$$\frac{dQ_{gfmi}}{dt} = \frac{3}{2} \left(v_{p\beta} \frac{di_{g\alpha}}{dt} + i_{g\alpha} \frac{dv_{p\beta}}{dt} - v_{p\alpha} \frac{di_{g\beta}}{dt} - i_{g\beta} \frac{dv_{p\alpha}}{dt} \right)$$
(10)

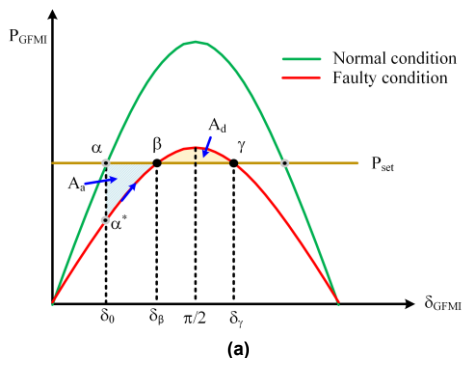
By inserting (5), (6), (7), and (8) in to (9) and (10), and making the derivative of active and reactive power equal to zero, the dynamics in active and reactive powers are obtained as.

$$P_{gfmi} = \frac{3}{2} \frac{V_{ac}}{Z_I} \left[\left(V_{p0} \cos \delta_{gfmi} - V_{ac} \right) \cos \theta_I + V_{p0} \sin \theta_I \sin \delta_{gfmi} \right]$$
(11)

$$Q_{gfmi} = \frac{3}{2} \frac{V_{ac}}{Z_l} \left[\left(V_{p0} \cos \delta_{gfmi} - V_{ac} \right) \sin \theta_l - V_{p0} \cos \theta_l \sin \delta_{gfmi} \right]$$
 (12)

where Z_l and θ_l are the impedance and phase of the line impedance between the GFMI and the common AC. Considering the effect of line impedance between the GFMI and the ac bus to be more inductive in nature and dominating than the resistive part. Then, (11) and (12) are simplified as,

$$P_{gfmi} = \frac{3}{2} \frac{V_{ac} V_{pcc} \sin \delta_{gfmi}}{j \omega L_{line}}$$
 (13)



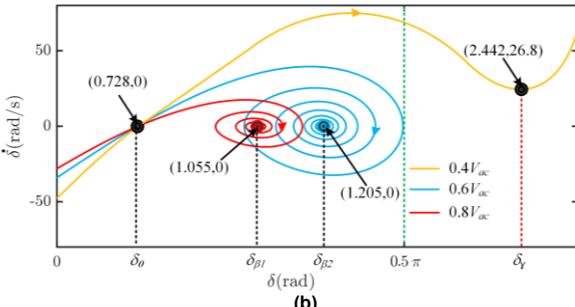


FIGURE 1. Transient stability analysis for the GFMIs under the large-scale disturbance (a) PGFMI- δ_{gtmi} curve under normal and faulty condition, (b) phase portrait of GFMI under the different magnitudes of the impact from fault.

$$Q_{gfmi} = \frac{3}{2} \frac{V_{ac} V_{pcc} \cos \delta_{gfmi} - V_{ac}}{j\omega L_{line}}$$
(14)

By inserting (13) in to (1) and taking the derivative of the resulting relation, the dynamics of the voltage angle of the GFMI is given by,

$$\dot{\delta}_{gfmi} = \omega_0 + d_p \frac{\omega_c}{s + \omega_c} (P_{set} - \frac{3}{2} \frac{V_{ac} V_p \sin \delta_{gfmi}}{\omega_0 L_{line}}) = \omega_{gfmi}$$
 (15)

where ω_{gfmi} is the instantaneous frequency of GFMI generated via power-frequency loop of droop control. Now by applying the differentiation to (15) that will derive a second-order differential equation for the voltage angle dynamics, and it is given by,

$$\ddot{\delta}_{gfmi} = d_p \omega_c (P_{set} - \frac{3}{2} \frac{V_{ac} V_p \sin \delta_{gfmi}}{\omega_0 L_{ting}}) - \omega_c \dot{\delta}_{gfmi}$$
(16)

Resultantly, the large-signal dynamic model for the voltage angle is used to analyze the angle's trajectory subject to the three-phase symmetrical short-circuit faults. Fig. 1 (a) illustrates the GFMI's output active power delivered with respect to voltage angle before and after disturbance created by a three-phase symmetrical short circuit fault. Due to this fault, the P_{GFMI} reduces, and the initial voltage angle (δ_0) will accelerate to increase P_{GFMI} and match the P_{set} . Then, voltage angle will decelerate and settle to a new equilibrium point If the acceleration area (A_a) is less than the deacceleration area (A_d) , GFMI can always find the new equilibrium point in the post-fault condition. However, as depicted in the phase portrait of GFMI in Fig. 1 (b), with the severity of the fault, drop in common AC voltage increases and so does the voltage angle in the post-fault condition. Specifically, when V_{ac} drops to 0.8 p.u., the δ_0 changes from



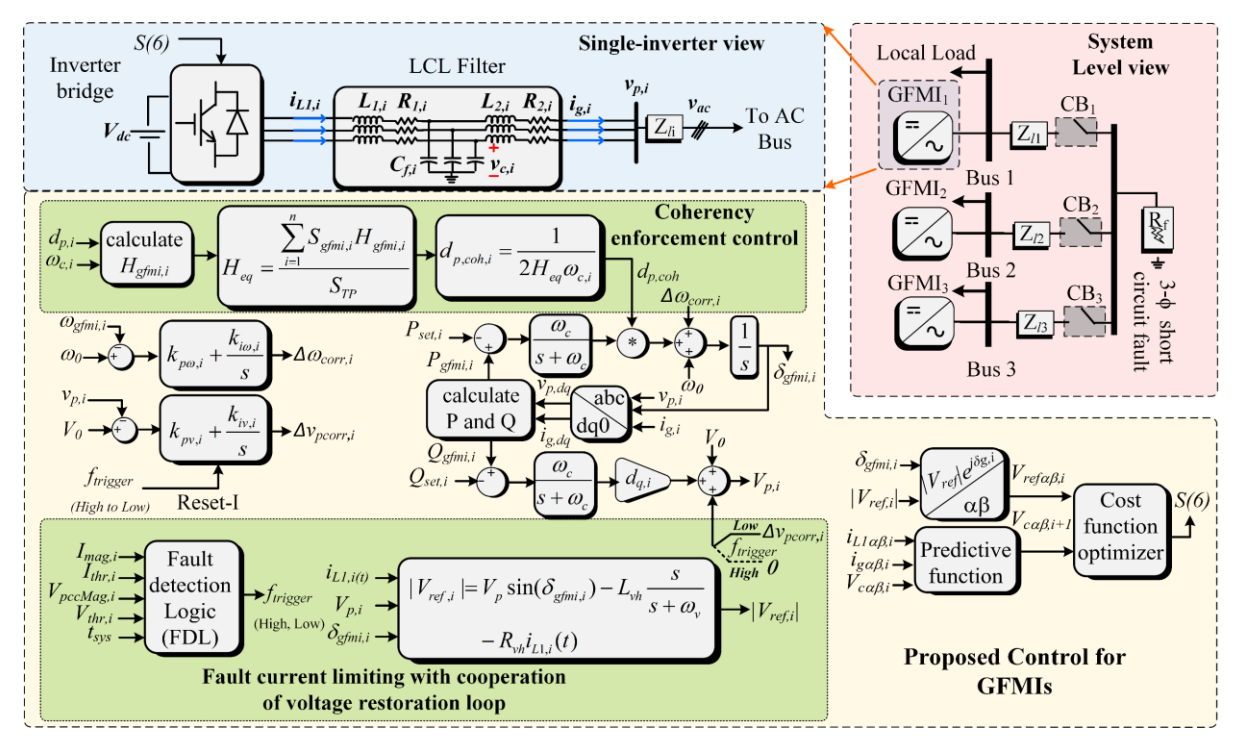


FIGURE 2. Structure of proposed control and the system level view of understudy PEDG comprised of droop-controlled GFMIs

0.728 rad to 1.055 rad, and for 0.6 p.u. V_{ac} the change in voltage angle is even more and new voltage angle ($\delta_{\beta 2}$) reaches to 1.205 rad. Furthermore, oscillations in the GFMI's voltage angle are also increased. In this case, when V_{ac} drops to 0.4 p.u. during the fault, the voltage angle crosses the critical angle (δ_{Y}) which is 2.442 rad. Thus, the A_{a} becomes greater than the A_{d} and the angle fails to find the equilibrium point and keeps on accelerating even in post-fault condition. This will cause transient instability and loss of synchronism for GFMI under large-scale disturbance.

III. FORMULATION OF RESILENT CONTROL FOR GFMI

The structure of the resilient control for GFMI in low inertia power system and the architecture of the understudy PEDG are depicted in Fig. 2. The system level view shows the understudy PEDG is comprised of heterogeneous GFMIs with their respective local loads and is interfaced with a shared common AC bus. As the system considered doesn't include generation from SGs and no interconnections with an upper network or a large power system, thus, it is inherently a low inertia power system. In this control, GFMIs are controlled via droop-based control interfaced with a model predictive control (MPC). MPC is utilized to regulate the voltage reference generated via droop control. To improve the resiliency of these droop controlled GFMIs for the fault ride through operation, two additional control blocks in the primary control for GFMIs are implemented. Specifically, coherency enforcement control and a fault current limiting scheme are adopted.

A. COHERENCY ENFORCEMENT CONTROL

Although in this work authors have considered droop control based GFMIs but in the authors' previous works, the coherency was enforced considering heterogeneity in the controller structure for inverters in PEDG. For instance, in [31], VSG (virtual synchronous generator) based control for GFMIs was considered for enforcing coherency. In [32], the understudy PEDG was comprised of GFMIs whose primary control is either droop control or for some GFMIs the primary controller is based on VSG. Similarly, in [33], the coherency is enforced among inverters whose primary control was based on GFMI and GFLIs.

In the understudy low inertia PEDG as shown in Fig. 2, the coherency among the GFMIs is enforced via modifying each GFMI's droop gain related to active power and frequency. Utilizing the low-pass filter dynamics in (1), the droop-based control can inherently emulate virtual inertia. Thus, the equivalence between droop control equation and swing equation used in the basic control of the virtual synchronous generator can be formed [34]. The relation between the inertia constant and the related droop gains of each GFMI is given by,

$$H_{gfmi,i} = \frac{1}{2d_{n,i}\omega_{c,i}} \tag{17}$$

where i=1,2,3...n and is the index number for the GFMI. $H_{gfmi,i}$ is the inertia constant of GFMI. The equivalent inertia constant (H_{eq}) for PEDG comprised of n GFMIs is given as,

$$H_{eq} = \frac{\sum_{i=1}^{n} S_{gfmi,i} H_{gfmi,i}}{S_{TD}}$$
 (18)

where $S_{gfmi,i}$, and S_{TP} are the rated power of individual GFMI and the rated power of the PEDG. The analytical relation to calculate modified droop gains is derived by equating to the equivalent inertia constant of the cluster and is given as,



$$d_{p,coh,i} = \frac{1}{2H_{eq}\omega_{c,i}} \tag{19}$$

where the $d_{p,coh,i}$ is defined as the modified droop gain that will ensure the coherency in the dynamic response of each GFMI in the cluster. The reference voltage magnitude and reference voltage angle generated via coherency enforcement control are regulated via MPC. The MPC is based on predicting the one step-ahead value of the controlled variable. In this work, the output voltage of GFMI is regulated according to the reference generated for GFMI via incorporating coherency enforced control parameters. The state space model of GFMI is depicted in Fig. 2 and derived via applying KCL and KVL circuit analysis on the model of GFMI interfaced with LCL filter. State-space model in the continuous time domain for the i-th GFMI interfaced with LCL filter [35] is given by,

$$\frac{d}{dt} \begin{bmatrix} i_{L1,i} \\ v_{c,i} \\ i_{g,i} \end{bmatrix} = A_i \begin{bmatrix} i_{L1,i} \\ v_{c,i} \\ i_{g,i} \end{bmatrix} + B_i \begin{bmatrix} v_{inv,i} \end{bmatrix} + D_i \begin{bmatrix} v_{p,i} \end{bmatrix}$$
(20)

where, i is defined as the index for number of GFMIs in understudy PEDG, $i_{Ll,i}$ is referred as the converter-side current, $i_{g,i}$ is the output current, $v_{c,i}$ is denoted as the measured voltage at filter capacitor, $v_{inv,i}$ is the bridge voltage of converter, and $v_{p,i}$ is the point of common coupling voltage. A_i , B_i , and D_i are the system matrix, input matrix and feedforward matrix in continuous time domain, respectively, and these are given by,

$$A_{i} = \begin{pmatrix} -\frac{R_{1,i}}{L_{1,i}} & -\frac{1}{L_{1,i}} & 0\\ \frac{1}{C_{f,i}} & 0 & -\frac{1}{C_{f,i}}\\ 0 & \frac{1}{L_{2,i}} & -\frac{R_{2,i}}{L_{2,i}} \end{pmatrix}, B_{i} = \begin{pmatrix} 1/L_{1,i}\\ 0\\ 0 \end{pmatrix} \text{ and } D_{i} = \begin{pmatrix} 0\\ 0\\ -\frac{1}{L_{2,i}} \end{pmatrix}$$

where $R_{I,i}$, $R_{2,i}$, $L_{I,i}$, $L_{2,i}$, and $C_{f,i}$ are the *LCL* filter's passive elements. After applying discretization on (20), the one stepahead values of the state variables in considered system in stationary reference frame ($\alpha\beta$) are given by,

$$\begin{bmatrix} i_{L1\alpha\beta,i,k+1} \\ v_{c\alpha\beta,i,k+1} \\ i_{g\alpha\beta,i,k+1} \end{bmatrix} = A_{disc,i} \begin{bmatrix} i_{L1\alpha\beta,i,k} \\ v_{c\alpha\beta,i,k} \\ i_{g\alpha\beta,i,k} \end{bmatrix} + B_{disc,i} \begin{bmatrix} v_{inv\alpha\beta,i,k} \\ \end{bmatrix} + D_{disc,i} \begin{bmatrix} v_{n\alpha\beta,i,k} \\ v_{n\alpha\beta,i,k} \end{bmatrix}$$

$$(21)$$

where, system matrix $A_{disc,i}$, input matrix $B_{disc,i}$, and feedforward matrix $D_{disc,i}$ are the discretized form that can be derived by,

$$\begin{aligned} A_{disc,i} &= e^{A_{i}T_{s}}, \ B_{disc,i} &= \int_{0}^{T_{s}} e^{A_{i}\tau} d\tau B_{i} = \left[\frac{e^{A_{i}\tau}}{A_{i}}\right]_{0}^{I_{s}} \\ B_{disc,i} &= A_{i}^{-1} \left(A_{disc,i} - I\right) B_{i}, \ D_{disc,i} &= A_{i}^{-1} \left(A_{disc,i} - I\right) B_{i} \end{aligned}$$

The implemented predictive control predicts the value of the voltage based on converter-side inductor current, capacitor voltage and grid-side inductor current. Then, based on the discretized state-space model devised in (21), and the system inputs, the one-step ahead capacitor voltage is predicted. The cost function optimization block compares and minimizes the cost function given as,

$$g = |\vec{v}_{refa\beta,i,k} - \vec{v}_{ca\beta,i,k+1}|$$

$$\vec{v}_{ca\beta,k+1} = \vec{v}_{ca,k+1} + j\vec{v}_{c\beta,k+1}$$

$$S_{k+1} = \arg\min(g)$$
(22)

where, $\vec{V}_{ref,\alpha\beta,k}$ is the reference voltage vector in stationary reference frame and the $\vec{V}_{c,\alpha\beta,k+1}$ is the predicted capacitor voltage vector. The switching state vector that minimizes (22) will be selected as the optimized switching state vector and then it is fed to the inverter bridge. Furthermore, as in a droop-based primary controller, the frequency and voltage are set to different levels after the disturbance. Therefore, a PI-based controller is used to bring the voltage and the frequency back to the nominal value. This control has a similar operation as a frequency governor and automatic voltage regulator have in SG. The mathematical model of this controller is given by,

$$\Delta \omega_{corr,i} = k_{p\omega,i} (\omega_0 - \omega_{emfi,i}) + k_{i\omega,i} \int (\omega_0 - \omega_{efmi,i}) dt$$
 (23)

$$\Delta v_{pcorr,i} = k_{pv,i} (V_0 - v_{p,i}) + k_{iv,i} \int (V_0 - v_{p,i}) dt$$
 (24)

where, $\Delta\omega_{corr,i}$ and $\Delta\nu_{pcorr,i}$ are the correction terms for the frequency and the PCC voltage, $k_{p\omega,i}$ and $k_{i\omega,i}$ are the PI gains for the frequency restoration loop, and $k_{p\nu,i}$ and $k_{i\nu,i}$ are the PI gains for the voltage restoration loop. By incorporating the proposed coherency enforcement control, each GFMI's δ_{gfmi} will swing together in the disturbance due to the enforced coherency. Thus, the GFMI will not lose synchronism, and this will greatly enhance the transient stability of the PEDG. This claim is further validated via HIL-based experimental case studies.

B. OVERCURRENT LIMITING SCHEME WITH THE COOPERATION OF VOLTAGE RESTORATION LOOP

The implemented scheme for the overcurrent limitation of the GFMI during the fault is comprised of, (i) FDL module that detects the start and end of the fault, and (ii) an overcurrent limiting module that is coordinated with the FDL module and voltage restoration loop to restrict the high short circuit current during the fault. Each GFMI is equipped with the implemented overcurrent limiting scheme as a local controller. The FDL module in the proposed control is monitoring the output current and PCC voltage of the GFMI to detect the start of the fault and allows safe system restoration when the fault is cleared. Fig. 3 illustrates the FDL algorithm. As it is shown, the inputs to the FDL module are the output current threshold (I_{thr}) , the magnitude of the inverter-side current (I_{mag}) , the magnitude of PCC voltage (V_{pccMag}) , minimum PCC voltage threshold (V_{thr}) , and system clock (t_{sys}) variables. The FDL module has local variables that are defined as: α associated with upper current limit hit flag, β is the voltage restoration start flag, γ stores the system clock when I_{mag} becomes less than the I_{thr} , λ is the lower current limit hit flag. The constant B is denoted as the



FDL local variable defination:

 α : upper current limit hit flag β : voltage restoration start flag γ : stores the system clock when λ becomes one λ : lower current limit hit flag

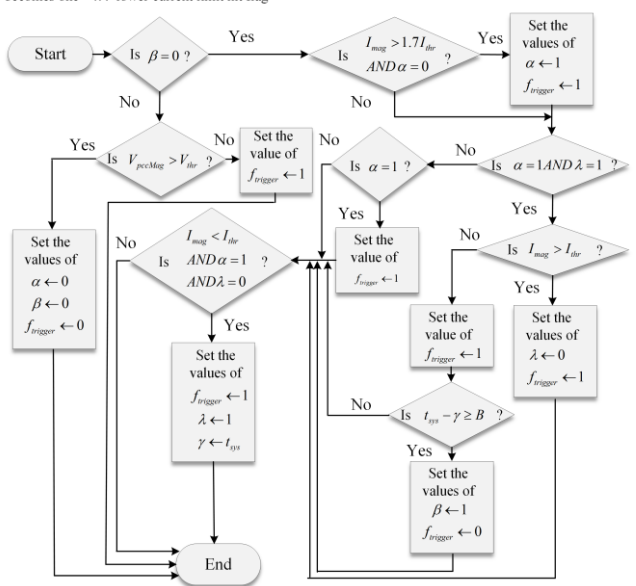


FIGURE 3. Description of the fault detection logic (FDL) algorithm

TABLE II. SYSTEM SPECIFICATIONS

TABLE III OTOTEM OF ESHIOATISMS			
Parameters	Value & units		
Nominal power of GFMI ₁ , GFMI ₂ , GFMI ₃ ,	10.5, 9.2, 8.0 kW		
Inverter-side filter inductor L_{11} , L_{12} , L_{13} ,	5, 4.5, 3.8 mH		
Grid-side filter inductor L_{21} , L_{22} , L_{23}	3.25, 2.75, 2.25 mH		
Filter Capacitor C_{f1} , C_{f2} , C_{f3}	$69, 63, 57 \mu F$		
Controller gains dp_1, dp_2, dp_3 Calculated controller gains $d_{p1,coh}, d_{p2,coh}, d_{p3,coh}$ DC Link voltage V_{dc}	(1.2, 0.8, 0.5) x10 ⁻³ rad/s/W (0.84, 1.4, 0.62) x10 ⁻³ rad/s/W 400 V		
Sampling time T_s	50 μs		
Magnitude of PCC Voltage V_{pccMag}	120 V		
Minimum PCC voltage threshold V_{thr}	108 V		
Magnitude of threshold current I_{thrl} , I_{thr2} , I_{thr2} , I_{thr3} Vritual resistance R_{vh1} , R_{vh2} , R_{vh3}	29.2, 25.6, 22.2 A 0.51, 0.66, 0.71 Ω		
Virtual inductance $L_{vhl}, L_{vh2}, L_{vh3}$ Fault resistance R_{fault}	$0.0051,0.0058,\ 0.0064\ \mathrm{mH}$ 1 Ω		

minimum required time window during which the I_{mag} remains less than I_{thr} , this is implemented to prevent false fault-clearing signal. All the local variables in the FDL function are initialized to zero and B is initialized as half of the period of PCC voltage.

If the inverter current of GFMI becomes more than 1.5 times of threshold current α and $f_{trigger}$ become one and the routine starts to decrease the PCC voltage of GFMI to prevent the overcurrent. This trigger signal is then fed to the proposed control to stop the action of the voltage restoration scheme during the fault. This makes the current limitation scheme to be more effective in reducing the current below the threshold current. When the fault is cleared, and the system must be restored to normal operation, the FDL checks two conditions. The 1^{st} condition is that the I_{mag} is less than

 I_{thr} and an extension to this condition is that it should hold for half of the system cycle. If this condition is fully met, then the system starts to restore the voltage. However, to prevent the system from incorrectly disabling the voltage restoration loop in post-fault conditions, another condition that needs to be considered is that the V_{pccMag} should be greater than V_{thr} . If this condition holds, then $f_{trigger}$ signal becomes zero and the integrator of voltage restoration is reset, and system is successfully restored to normal conditions. This logic is summarized in the algorithm illustrated in Fig. 3.

Since the short-circuit fault negatively impacts the voltage of the common AC bus between the GFMIs, therefore, the PCC voltage of the GFMI must be lowered accordingly to limit the overcurrent during the fault. Therefore, the following equation is used to modify the voltage reference during fault that modifies the magnitude of the voltage reference, and this relationship is given by,

$$|V_{ref,i}| = V_p \sin(\delta_{gfmi,i}) - R_{vh} i_{L1,i}(t) - L_{vh} \frac{s}{s + \omega_{i}}$$
 (25)

where, $|V_{ref,i}|$ is the modified magnitude of the voltage reference, V_p is the magnitude of the voltage reference, where ω_v is selected to mitigate high-frequency components of current on the reference voltage frequency of current R_{vh} and L_{vh} are selected to meet the following condition for the current

$$\left|I_{max,i}\right| \ge \sqrt{I_{L1,\alpha,i}^{2} + I_{L1,\beta,i}^{2}}$$
 (26)

where $I_{\max,i}$ is the maximum magnitude of tolerable current for i^{th} GFMI, $I_{LI,a,i}$ and $I_{LI,\beta,i}$ are the value of inverter side inductor in $\alpha\beta$ frame, respectively.

IV. IMPACT ANALYSIS OF DIFFERENT COHERENCY LEVELS IN PEDG DURING FAULT

This impact analysis is performed via quantizing the heterogeneity level of the GFMIs in PEDG and it will provide insights into the amount of acceleration of effective voltage angles during fault. Notably, with the help of analytical simulation results it will be shown that different heterogeneity levels can increase or decrease the difference of effective voltage angles from initial synchronized state. Therefore, the impact of short-circuit fault is studied with varying the level of coherency among the GFMIs. The level of coherency among the GFMIs is determined via coherency factor (COF) and it is given by,

$$COF = \sqrt{\sum_{i=1}^{n} (H_{eq} - H_i)^2}$$
 (27)

according to (27), the higher the value of COF refers to the higher deviation from the coherency and the smaller value of COF denotes the GFMIs are converging towards coherency. For the fully coherent case, the value of COF is zero. Thus, to test the advantage of enforcing the GFMIs to be coherent in fault, at instant t_1 , a short circuit fault occurred between bus #1 and #2, and this fault lasted till time instant t_2 . Five scenarios are simulated with different COFs that are achieved by varying the parameters of GFMI. Initial values of parameters used to



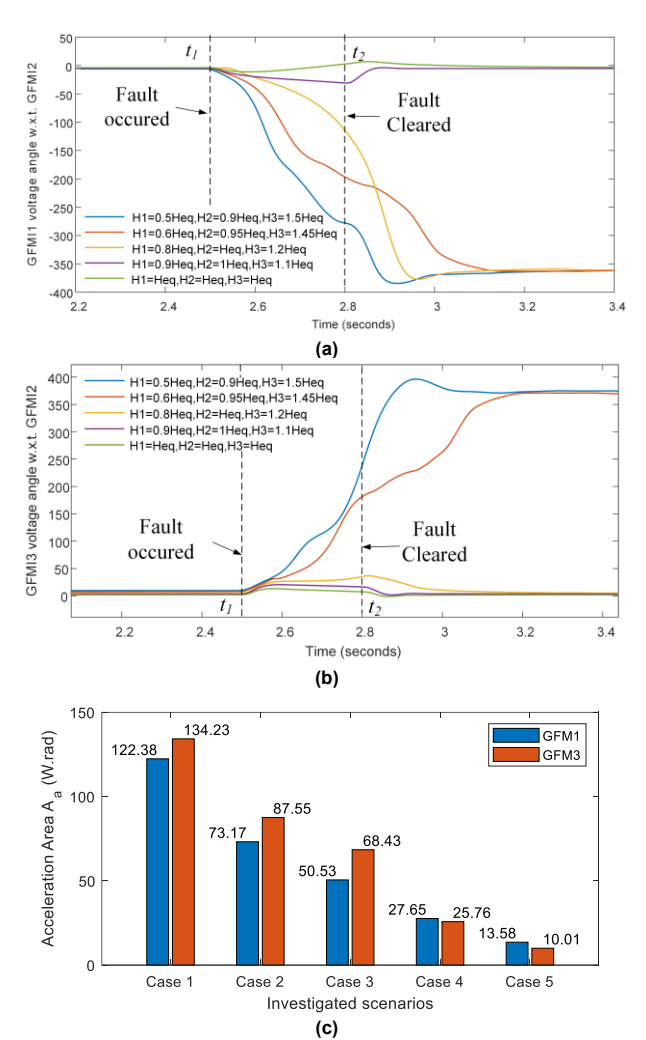
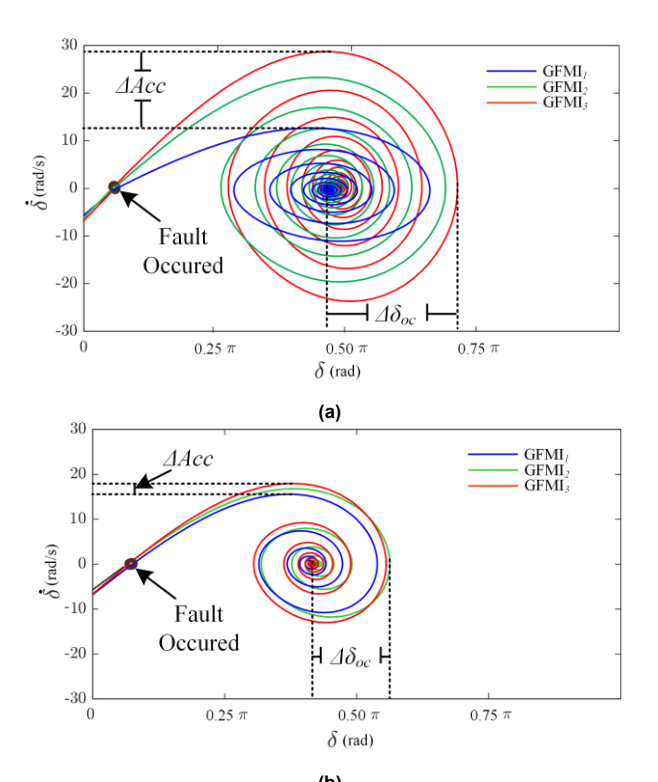


FIGURE 4. Effect of varying the level of coherency in PEDG on the voltage angles of GFMIs during the short circuit fault (a) GFMI1 voltage angle with respect to GFMI2, (b) GFMI3 voltage angle with respect to GFMI2, and (c) Acceleration area (Aa) of GFMI1 and GFMI3 with respect to GFMI2

model the GFMIs in the considered PEDG network are provided in Table I.

Fig. 4 (a) and (b) illustrate the dynamics of GFMI₁ and GFMI₃ voltage angles with respect to GFMI₂ with varying the level of coherency in considered low inertia PEDG. It can be verified from Fig. 4 that case 1(blue plot) is the most noncoherent as each GFMI's inertia constants are specified as $H_1=0.5H_{eq}$, $H_2=0.9H_{eq}$, and $H_3=1.6H_{eq}$ and COF is calculated as 0.73. In such a case, the deviation in the voltage angle of GFMI₁ and GFMI₃ with respect to GFMI₂ during the fault is highest. Specifically, for GFMI₁ the voltage angle with respect to GFMI₂ changes during the fault from -6° to -279.8° and in post-fault condition settles to -360°. Moreover, for GFMI₃, the voltage angle with respect to GFMI₂ changes from 1.5° to 239.1° and finally settles to +360° in a post-fault condition. In the 2nd scenario (red plot) when the GFMIs have inertia constants $H_1=0.6H_{eq}$, $H_2=0.95H_{eq}$, and $H_3=1.45H_{eq}$, the voltage angle experiences significantly lesser change during the fault as compared to the previous case. Precisely, the GFMI₁'s voltage angle with respect to GFMI₂ experience



(b) FIGURE 5. Phase portraits of GFMI under fault in: (a) a non-coherent network of GFMIs, and (b) coherency enforced network of GFMI with proposed control.

changes from -1.5° to -187° during the fault and settles to -360° in the post-fault steady-state condition. Similarly, the GFMI₃'s voltage angle with respect to GFMI₂ changes from 2.5° to 182.5° and settles to 360° in post fault state. Similarly, as the GFMIs level of coherency is increased the value of COF becomes smaller. Moreover, the voltage angle deviation during the fault decreases. For the fully coherent case V (green plot) the COF is calculated as zero. Specifically, for GFMI₁ the voltage angle with respect to GFMI₂ changes from -2.91° to +6.86° during the fault, and in post fault steady-state the voltage angle returns to -2.91°. Furthermore, for GFMI3 the voltage angle with respect to GFMI₂ changes from 1.68° to 7.44° during the fault, and as the fault is cleared the voltage angle returns to 1.68°. Thus, this validates that with a fully coherent cluster of GFMIs, the voltage angles during faults experience minimum deviations. Moreover, in the post fault scenario, the voltage angle regains its previous value of angle, which is the initial equilibrium point. Furthermore, Fig. 4 (c) depicts the acceleration area of the voltage angle GFMIs (see Fig.1 (a)) during the fault. It can be verified that for noncoherent scenario (case 1) A_a is the highest for GFMI₁ and GFMI₃ is 122.38 (*W.rad*) and 134.23 (*W.rad*). As the level of coherency is increased the area of acceleration is reduced significantly, for instance, in case 5 for the fully coherent cluster of GFMIs, the area of acceleration for GFMI₁ and GFMI₃ is mere 13.58 (*W.rad*) and 10.01 (*W.rad*), respectively.

Fig. 5 (a) in the revised manuscript shows the phase portraits of the non-coherent GFMI under three-phase short circuit fault. As shown when a fault occurs the voltage angle



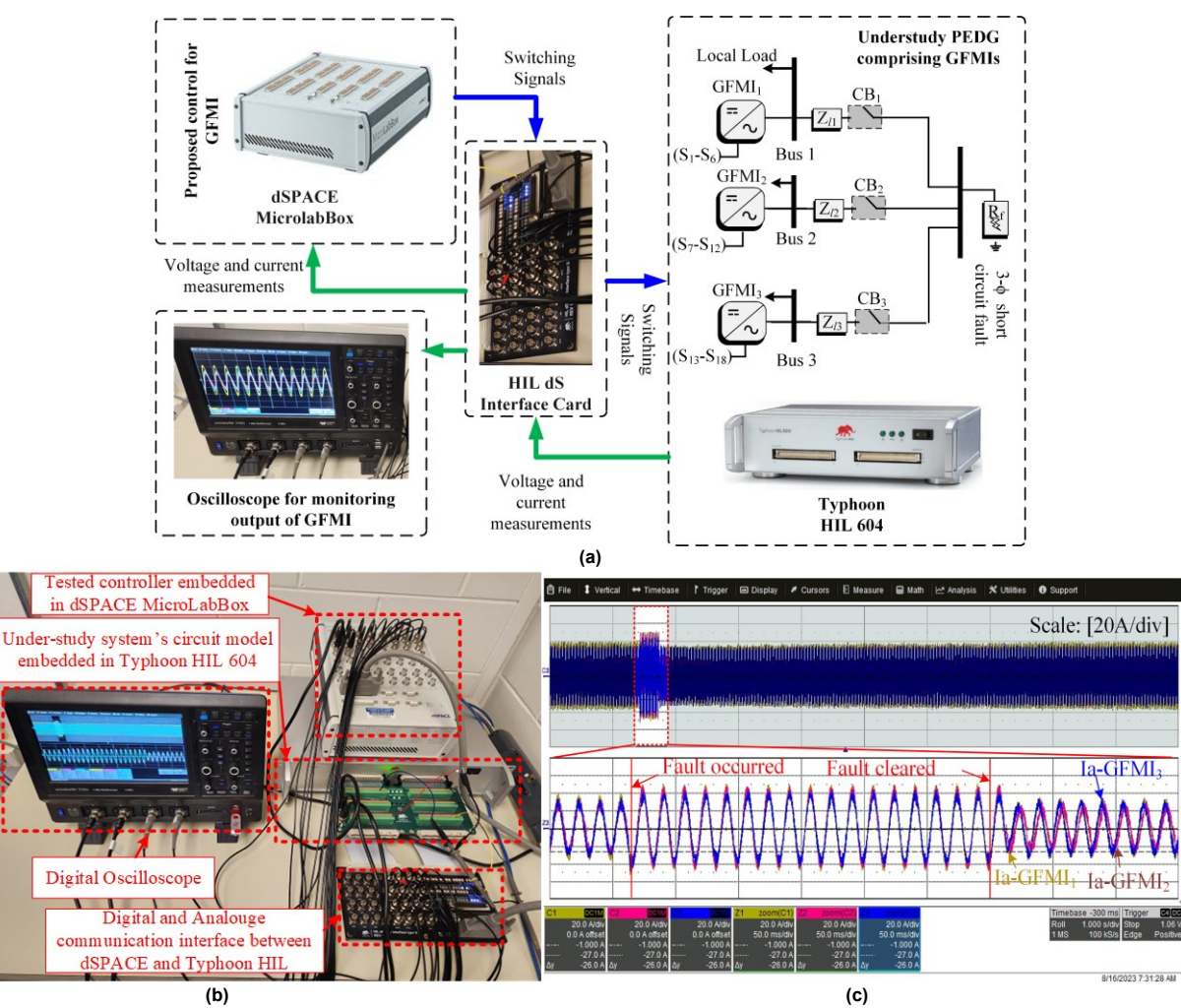


FIGURE 6. Hardware-in-the-loop (HIL) setup to experimentally validate the proposed scheme: (a) main power circuit schematics of the HIL setup, (b) Actual built setup, and (c) digital oscilloscope's snapshot that illustrates the phase A of output current of GFMIs with proposed control in pre-fault, during fault and post-fault state.

of GFMI starts to accelerate, and it can be noticed that each GFMI has a distinct acceleration that relates to the noncoherent dynamic behavior. Specifically, the difference between the accelerations ($\triangle Acc$) of GFMI₁ (having smallest angle acceleration) and GFMI3 (that exhibits largest acceleration) is 18.5 rad/s. Moreover, GFMI₂ and GFMI₃ have large oscillations while reaching an equilibrium point. Significantly, the largest positive oscillations ($\Delta \delta_{oc}$) from the equilibrium point are exhibited by GFMI₃ and it is $0.26 \pi rad$. These large oscillations of the voltage angle can pose severe threats to the stability of understudy power grid as voltage angle may cross the critical angle and resultantly the effected GFMI can lose the synchronism due to transient instability. Comparatively, with the proposed coherency enforcement scheme, it is illustrated in Fig. 5 (b) of the revised manuscript that under the fault each GFMI's voltage angle swing together with minimal acceleration differences i.e. ΔAcc is 1.5 rad/s and it prevents the large oscillations while reaching an equilibrium point as the $\Delta \delta oc$ is 0.085π which is three times less than the non-coherent GFMIs. Thus, this validates that having high level of coherency among the heterogeneous

GFMIs will facilitate the resilient operation of GFMI during the fault via inhibiting the large acceleration of voltage angles from the initial synchronized state and increase chances of regaining the original equilibrium point.

V. HARDWARE-IN-THE-LOOP (HIL) EXPERIMENTAL RESULTS

The proposed control scheme is tested via an HIL experimental setup as depicted in Fig. 6. The controller is embedded in the dSPACE microLabBox and the low inertia PEDG comprising of three GFMIs is modelled in Typhoon HIL 604. HIL- dSPACE communication interface is used to achieve communication between the two devices. The analog signals that consist of measurements of the inverterside current, output current, and PCC voltage are sent to the dSPACE microLabBox from Typhoon HIL 604. Moreover, the respective digital switching signals for each GFMI are sent to the Typhoon HIL from the dSPACE microLabBox. The system specifications are given in Table II. The short fault is applied for duration of 0.3s on PEDG and the impact of this fault is analyzed with non-coherent GFMIs, partially



coherent GFMI cluster, and enforced coherent GFMIs via proposed control.

A. CASE STUDY I: HETEROGENEOUS AND NON-COHERENT CLUSTER OF GFMIS WITHOUT PROPOSED CONTROL

In this case study, the PEDG comprised of heterogeneous GFMIs that exhibit non-coherent behavior during the disturbance. Specifically, the COF for these GFMIs is calculated to be 0.75, that is non-zero. At instant t₅, a short circuit fault occurred between bus #1 and bus #2, and at t6, the fault was cleared. Fig. 7 (a) illustrates the RMS of the PCC voltage of each GFMI in pre-fault, during fault (zoomed), and post-fault state. In pre-fault state, all the GFMIs have PCC voltage at 120 V RMS. However, at instant t5, the fault occurs and the PCC voltage of GFMI drops rapidly to 60 V, 62 V, and 72 V. Thus, this will lead to the sudden increase of the output current from each GFMI. However, due to conventional overcurrent protection, the current is limited as shown in Fig. 7 (b). This will impact the active power output of each GFMI, and it can be seen in the zoom-in window of Fig. 7 (c) that for GFMI1 the active power is dropped from 8782 W to 5689 W, for GFMI2 the active power is changed from 7246 W to 5538 W and for GFMI3 the active power is limited to 4597 W that was 6263 W in a pre-fault state. This reduction in active power will lead to an increase in the voltage angles to match the nominal active power. Fig. 7 (d) shows the frequency of each GFMI, and it can be seen that the frequency of each GFMI is increased due to the voltage angle acceleration. Since the GFMIs are non-coherent, each GFMI has a different frequency dynamic response during the transients. As the voltage angle between each GFMI is changing differently these GFMIs are deviating from the initial synchronization. Moreover, this impact can also be seen in the reactive power. Fig. 7 (e) depicts the reactive power profile of each GFMI, and during the fault, as the PCC voltage suddenly reduces the voltage restoration scheme of each GFMI acts to restore the voltage. In the post-fault state, at instant t6 when the fault is cleared, significant oscillations in the RMS of output current, RMS of PCC voltage, active power, frequency, and reactive power are observed. These oscillations are happening due to the angle deviations between the GFMIs that occurred during the fault. Therefore, this can impact the transient stability of GFMI and forces the system to find a new equilibrium point. Thus, this will take around 11.2 sec for the system to fully restore and reach the new equilibrium point.

B. CASE STUDY II: HETEROGENEOUS AND PARTIALLY COHERENT CLUSTER OF GFMIS WITHOUT FDL COORDINATION

This case study refers to the heterogeneous cluster of GFMIs that are partially coherent. The coherency factor for this case is calculated to be 0.28 which is less than the previous case but not zero. Fig. 8 (a) illustrates the impact of fault on the RMS of PCC voltage of each GFMI. At instant t_7 the fault occurred and the RMS of PCC voltage for GFMIs decreased to 66 V, 60.27 V, and 68.75 V, respectively.

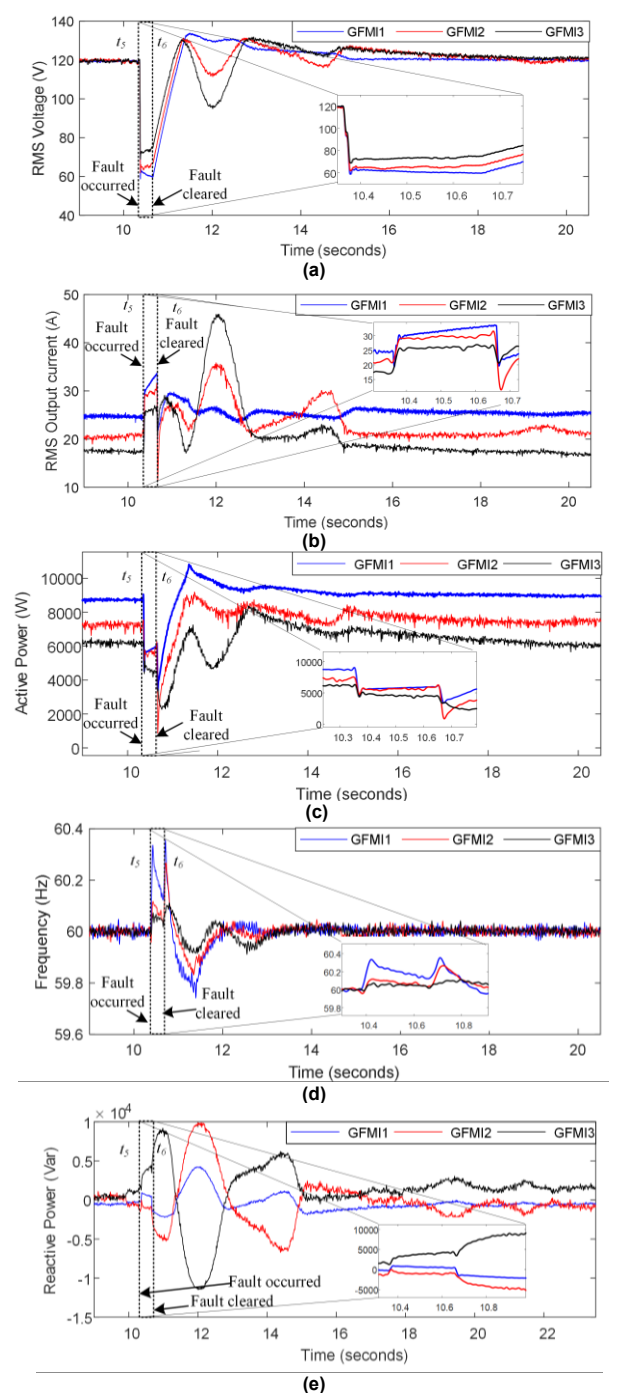


FIGURE 7 Case study I: a PEDG comprising non-coherent GFMIs without proposed control under the short circuit fault between bus # 1 and #2; (a) RMS of PCC voltage, (b) RMS of output current, (c) active power profile, (d) frequency of GFMIs, and (e) reactive power profile.

Therefore, this led to a sudden increase in the output current as shown in Fig. 8 (b). The RMS value of the output current of each GFMI is limited during the fault. Resultantly, the active power output from each GFMI decreases during the fault. Specifically, Fig. 8 (c) illustrates the active powers of GFMI₁-GFMI₃ are limited to 6863.89 W, 4926.15 W, and 3705.96 W, respectively. That affects the voltage angle of each GFMI and these start to deviate away from each other. Fig. 8 (d) depicts the frequency of each GFMI, and the



zoomed plot shows the frequency of GFMIs during the fault. As the GFMIs are partially coherent, each GFMI has a different frequency dynamic response. Fig. 8 (e) illustrates the reactive power profile, and the zoomed window shows the increase in the reactive power due to angle deviation. At instant t_8 , the fault is cleared, and it can be seen from Fig. 8 that the oscillations occur in the RMS of output current, active power output, frequency, and the reactive power of GFMIs. Comparatively, these oscillations are less than case study I. This is due to the less deviation of the voltage angle during the fault. Thus, this case study shows the benefit of increasing the level of coherency among the GFMIs during the large-scale disturbance.

C. CASE STUDY III: COHERENCY ENFORCED HETEROGENEOUS GFMIS WITH FDL COORDINATION

This case study includes the results of incorporating the proposed control scheme to enforce coherency among the initially non-coherent and heterogeneous cluster of GFMIs. Moreover, the proposed FDL module is utilized to effectively detect the start and end of the fault event. Then this signal is incorporated with the voltage restoration scheme to mitigate the effect of windup of integrators in post-fault state. The coherency factor for this case study is zero as all the GFMIs have been forced to behave coherently. Thus, this will prevent the voltage angle and frequency of each GFMI from deviating and accelerating. Fig. 9 (a) illustrates the RMS of the PCC voltages of the GFMIs and at instant to a short circuit fault occurred between bus #1 and bus #2. The PCC voltage of GFMI₁-GFMI₃ reduces sharply due to the fault. Resultantly, the RMS of the output current tends to increase. However, the output current during the fault remains below the overcurrent limit (1.5 times the threshold current) due to the proposed control. Specifically, the output currents of the GFMI1-GFMI3 are 31.53 A, 29.53 A, and 26.09 A, respectively (see Fig. 9 (b)). Conclusively, the active power output from each GFMI is reduced and is limited to 6360 W, 6140 W, and 5770 W, respectively as shown in Fig. 9 (c). As the effective output active power from each GFMI is limited during the fault state, the voltage angle of the GFMIs changes homogenously during the fault. Therefore, by enforced coherency among the GFMIs, all the GFMIs will have similar frequency dynamics during the fault. Fig. 9 (d) depicts the frequency profile of GFMIs and the zoom-in window that shows the duration in which the fault lasted. It is seen that each GFMI has approximately similar response during the disturbance and thus, the voltage angles of GFMIs doesn't have large deviations, and the system maintains initial synchronization within the cluster of GFMIs and remains at higher stable equilibrium point. Furthermore, during the fault, the reactive power remains under the limit due to the coordination with the voltage restoration loop (see Fig. 9 (e)). At t_{10} , the fault is cleared, and it is observed from Fig. 9 that the system maintains its initial equilibrium point. Moreover, for every GFMI in the grid cluster, RMS output current, active power, RMS PCC voltage, and reactive power don't experience oscillations after the fault is cleared.

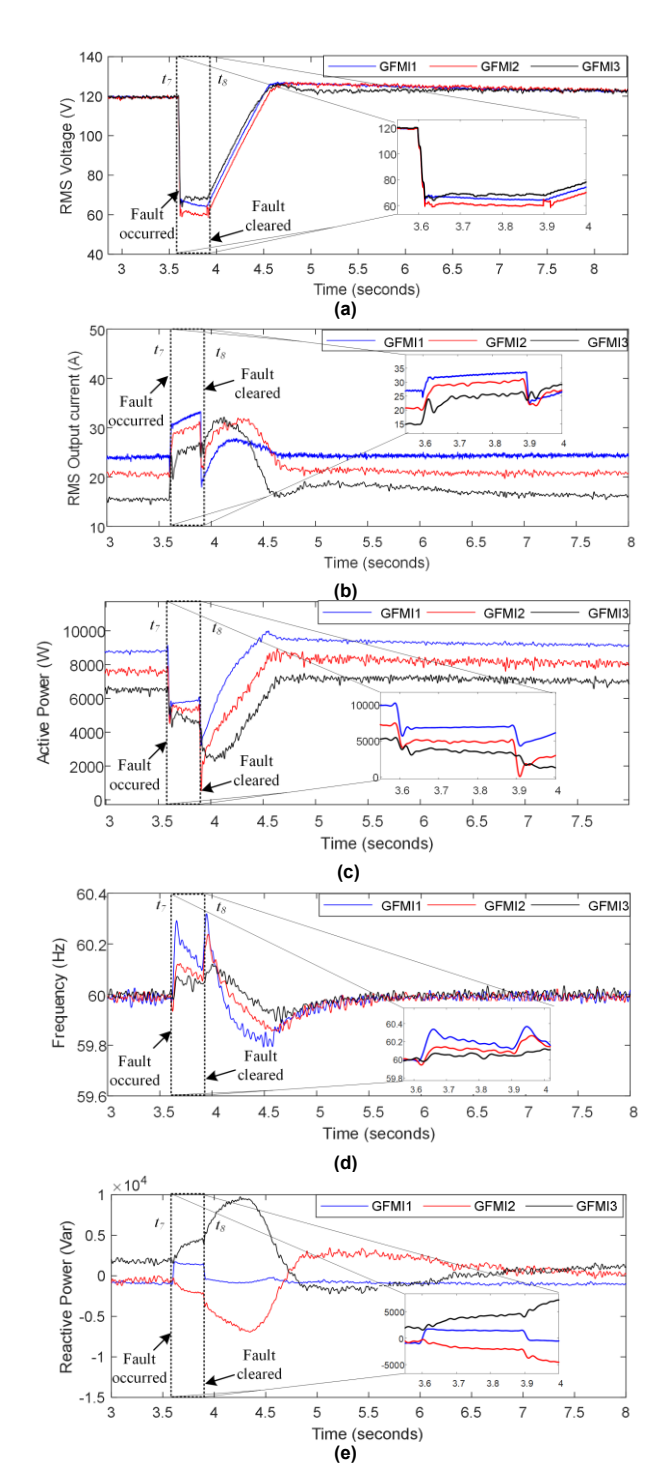


FIGURE 8 Case study II: a PEDG comprising partially coherent heterogeneous GFMIs without proposed control under the short circuit fault between bus # 1 and #2; (a) RMS of PCC voltage, (b) RMS of output current, (c) active power profile, (d) frequency of GFMIs, and (e) reactive power profile.

D. CASE STUDY IV: COHERENCY ENFORCED HETEROGENEOUS GFMIS WITH FDL COORDINATION UNDER FAULT WITH HIGHER SEVERITY

This case study concern applying a symmetric three phase short circuit fault with higher severity to assess the performance of the proposed scheme. Fig. 10 (a) illustrates



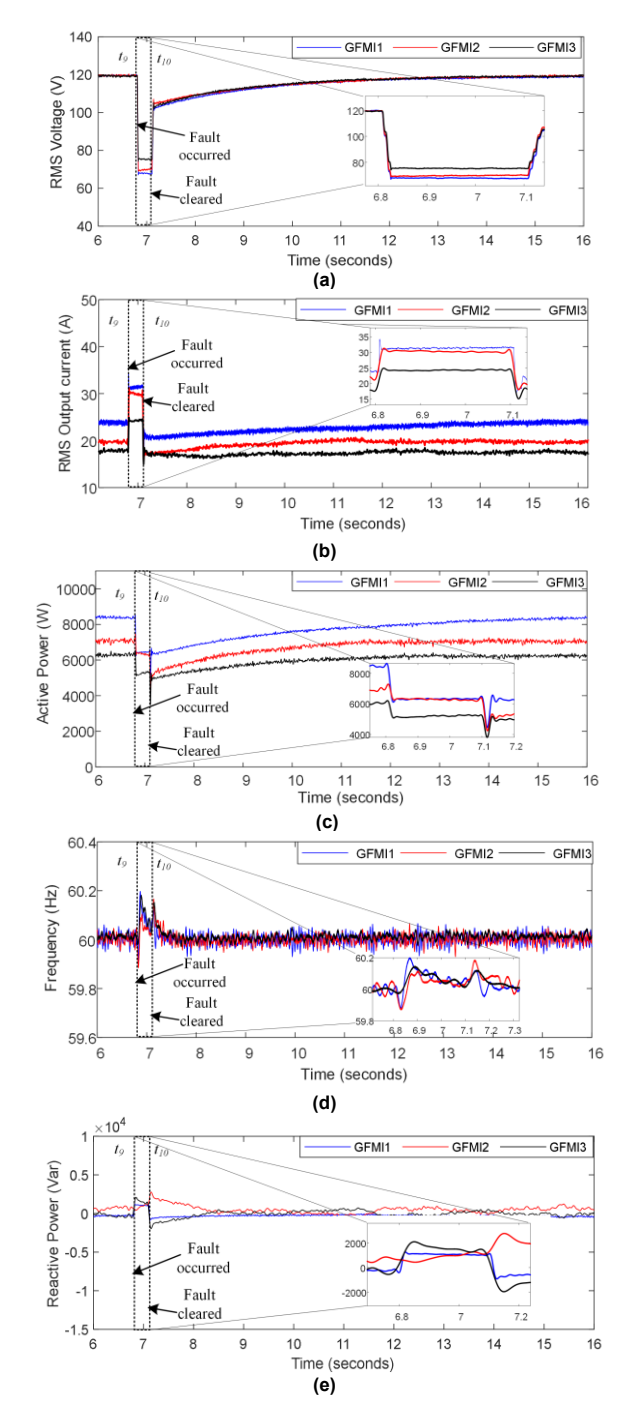


FIGURE 9 Case study III: a PEDG comprising enforced coherent GFMIs with proposed control under the short circuit fault between bus # 1 and #2; (a) RMS of PCC voltage, (b) RMS of output current, (c) active power profile, (d) frequency of GFMIs, and (e) reactive power profile.

the RMS value of the voltage during the fault and in post fault scenarios. At instant t_{11} , a symmetrical three phase fault is applied, and it impact the PCC voltage. Specifically, under fault RMS value of PCC voltage of GFMI1-3 is dropped rapidly to 32, 35, and 38, respectively. Moreover, when fault is cleared at instant t_{12} , the PCC voltage is restored to nominal value without oscillations. Similarly, Fig. 10 (b) shows the RMS value of the output current of each GFMI,

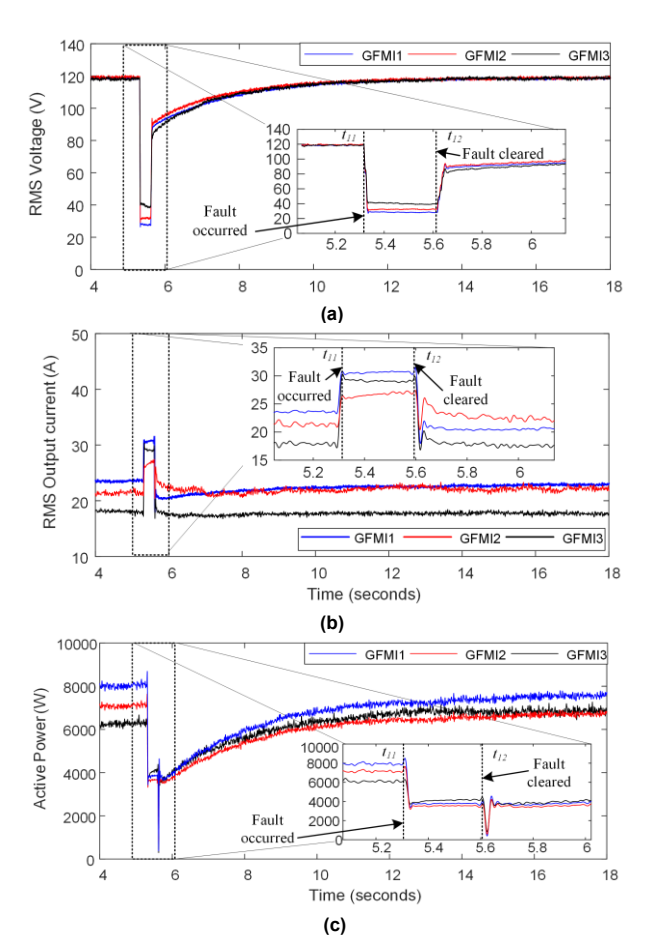


FIGURE 10 Case study IV: a PEDG comprising enforced coherent GFMIs with proposed control under short circuit fault between bus #1 and #2 increased severity; (a) RMS of PCC voltage, (b) RMS of output current, and (c) active power profile.

and it is verified that the current is restricted to the predefined threshold for each GFMI and when fault is cleared, a seamless transition towards normal conditions is ensued via proposed control. The active power profile is depicted in Fig. 10 (c) that also confirms a significant drop in the active power under the faulty conditions, but a smooth transition happened when fault is cleared, and normal conditions are restored. Thus, this case study verifies that even under increased fault severity the proposed control enables the understudy PEDG with a resilient operation. Therefore, it is concluded from these case studies that the proposed control scheme enables the low inertia PEDG to have better dynamic response during and post-fault state via minimal oscillations in the post-fault condition and revert to initial equilibrium that was in the pre-fault state.

VI. CONCLUSION

This paper proposed a control scheme that improves the resiliency and fault-tolerant operation of heterogeneous GFMIs in a low inertia PEDG. The intrinsic heterogeneity in the cluster of GFMI was mitigated via coherency enforcement between these GFMIs. The effect of increasing the level of coherency among the GFMIs during the large-scale disturbance, such as short circuit fault, was analyzed.



It was validated that with increasing the level of coherency, the operation of GFMI during the fault and in post-fault state is enhanced. Specifically, in the enforced coherent cluster of GFMIs, the voltage angles don't have large deviation from the initial synchronization, and in post fault state the large oscillations in the output current, PCC voltage, and active power are mitigated. The FDL module effectively detects the start and end of the fault state and enables the seamless transition from the fault to normal operation of GFMI. Moreover, the FDL module operates in collaboration with the voltage restoration scheme to enhance the effect of current limiting scheme during the fault and prevent the windup of voltage restoration loop. Various HIL case studies were conducted to validate the effectiveness of the proposed scheme and demonstrate the enhancement in the resilient operation of cluster of heterogeneous GFMIs during the large-scale disturbances.

REFERENCES

- S. Sajadian and R. Ahmadi, "Model Predictive Control of Dual-Mode Operations Z-Source Inverter: Islanded and Grid-Connected," *IEEE Transactions on Power Electronics*, vol. 33, no. 5, pp. 4488-4497, 2018, doi: 10.1109/TPEL.2017.2723358.
- [2] Q. Peng, Q. Jiang, Y. Yang, T. Liu, H. Wang, and F. Blaabjerg, "On the Stability of Power Electronics-Dominated Systems: Challenges and Potential Solutions," *IEEE Transactions on Industry Applications*, vol. 55, no. 6, pp. 7657-7670, 2019, doi: 10.1109/TIA.2019.2936788.
- [3] M. S. Eslahi, S. Vaez-Zadeh, R. Heydari, and J. Rodriguez, "Resiliency Enhancement Control of Converter Fed Smart Renewable Micro Grids Against Multiple Risks," *IEEE Transactions on Energy Conversion*, vol. 38, no. 2, pp. 1028-1039, 2023, doi: 10.1109/TEC.2023.3235994.
- [4] Y. Li, Y. Gu, and T. Green, "Revisiting Grid-Forming and Grid-Following Inverters: A Duality Theory," *IEEE Transactions on Power Systems*, 2022.
- [5] J. M. Guerrero, L. G. De Vicuna, J. Matas, M. Castilla, and J. Miret, "A wireless controller to enhance dynamic performance of parallel inverters in distributed generation systems," *IEEE Transactions on power electronics*, vol. 19, no. 5, pp. 1205-1213, 2004.
- [6] M. Torres and L. A. Lopes, "Virtual synchronous generator control in autonomous wind-diesel power systems," in 2009 IEEE Electrical Power & Energy Conference (EPEC), 2009: IEEE, pp. 1-6.
- [7] M. A. Awal and I. Husain, "Unified Virtual Oscillator Control for Grid-Forming and Grid-Following Converters," *IEEE Journal of Emerging and Selected Topics in Power Electronics*, vol. 9, no. 4, pp. 4573-4586, 2021, doi: 10.1109/JESTPE.2020.3025748.
- [8] F. Zhao, X. Wang, and T. Zhu, "Low-Frequency Passivity-Based Analysis and Damping of Power-Synchronization Controlled Grid-Forming Inverter," *IEEE Journal of Emerging and Selected Topics in Power Electronics*, vol. 11, no. 2, pp. 1542-1554, 2023, doi: 10.1109/JESTPE.2022.3218845.
- [9] M. Eskandari and A. V. Savkin, "On the Impact of Fault Ride-Through on Transient Stability of Autonomous Microgrids: Nonlinear Analysis and Solution," *IEEE Transactions on Smart Grid*, vol. 12, no. 2, pp. 999-1010, 2021, doi: 10.1109/TSG.2020.3030015.
- [10] D. Pan, X. Wang, F. Liu, and R. Shi, "Transient Stability of Voltage-Source Converters With Grid-Forming Control: A Design-Oriented Study," *IEEE Journal of Emerging and Selected Topics in Power Electronics*, vol. 8, no. 2, pp. 1019-1033, 2020, doi: 10.1109/JESTPE.2019.2946310.
- [11] S. Ghosh, M. S. El Moursi, E. F. El-Saadany, and K. Al Hosani, "Online coherency based adaptive wide area damping controller for transient stability enhancement," *IEEE Transactions on Power Systems*, vol. 35, no. 4, pp. 3100-3113, 2019.

- [12] M. Jonsson, M. Begovic, and J. Daalder, "A new method suitable for real-time generator coherency determination," *IEEE Transactions on Power Systems*, vol. 19, no. 3, pp. 1473-1482, 2004.
- [13] B. Mahamedi and J. E. Fletcher, "The equivalent models of grid-forming inverters in the sequence domain for the steady-state analysis of power systems," *IEEE Transactions on Power Systems*, vol. 35, no. 4, pp. 2876-2887, 2020.
- [14] A. D. Paquette and D. M. Divan, "Virtual impedance current limiting for inverters in microgrids with synchronous generators," *IEEE Transactions on Industry Applications*, vol. 51, no. 2, pp. 1630-1638, 2014
- [15] X. Wang, Y. W. Li, F. Blaabjerg, and P. C. Loh, "Virtual-impedance-based control for voltage-source and current-source converters," *IEEE Transactions on Power Electronics*, vol. 30, no. 12, pp. 7019-7037, 2014.
- [16] J. He and Y. W. Li, "Analysis, design, and implementation of virtual impedance for power electronics interfaced distributed generation," *IEEE Transactions on industry Applications*, vol. 47, no. 6, pp. 2525-2538, 2011.
- [17] K. O. Oureilidis and C. S. Demoulias, "A fault clearing method in converter-dominated microgrids with conventional protection means," *IEEE Transactions on Power Electronics*, vol. 31, no. 6, pp. 4628-4640, 2015.
- [18] I. Sadeghkhani, M. E. H. Golshan, J. M. Guerrero, and A. Mehrizi-Sani, "A current limiting strategy to improve fault ride-through of inverter interfaced autonomous microgrids," *IEEE Transactions on Smart Grid*, vol. 8, no. 5, pp. 2138-2148, 2016.
- [19] M. G. Taul, X. Wang, P. Davari, and F. Blaabjerg, "Current limiting control with enhanced dynamics of grid-forming converters during fault conditions," *IEEE Journal of Emerging and Selected Topics in Power Electronics*, vol. 8, no. 2, pp. 1062-1073, 2019.
- [20] E. Rokrok, T. Qoria, A. Bruyere, B. Francois, and X. Guillaud, "Transient Stability Assessment and Enhancement of Grid-Forming Converters Embedding Current Reference Saturation as Current Limiting Strategy," *IEEE Transactions on Power Systems*, vol. 37, no. 2, pp. 1519-1531, 2022, doi: 10.1109/TPWRS.2021.3107959.
- [21] E. Rokrok, T. Qoria, A. Bruyere, B. Francois, and X. Guillaud, "Transient stability assessment and enhancement of grid-forming converters embedding current reference saturation as current limiting strategy," *IEEE Transactions on Power Systems*, vol. 37, no. 2, pp. 1519-1531, 2021.
- [22] A. Gkountaras, S. Dieckerhoff, and T. Sezi, "Evaluation of current limiting methods for grid forming inverters in medium voltage microgrids," in 2015 IEEE Energy Conversion Congress and Exposition (ECCE), 2015: IEEE, pp. 1223-1230.
- [23] N. Baeckeland, D. Chatterjee, M. Lu, B. Johnson, and G.-S. Seo, "Overcurrent Limiting in Grid-Forming Inverters: A Comprehensive Review and Discussion," *IEEE Transactions on Power Electronics*, 2024
- [24] N. S. Gurule, J. Hernandez-Alvidrez, R. Darbali-Zamora, M. J. Reno, and J. D. Flicker, "Experimental evaluation of grid-forming inverters under unbalanced and fault conditions," in *IECON 2020 The 46th Annual Conference of the IEEE Industrial Electronics Society*, 2020: IEEE, pp. 4057-4062.
- [25] B. Fan, T. Liu, F. Zhao, H. Wu, and X. Wang, "A review of current-limiting control of grid-forming inverters under symmetrical disturbances," *IEEE Open Journal of Power Electronics*, 2022.
- [26] J. Erdocia, A. Urtasun, and L. Marroyo, "Dual Voltage-Current Control to Provide Grid-Forming Inverters With Current Limiting Capability," *IEEE Journal of Emerging and Selected Topics in Power Electronics*, vol. 10, no. 4, pp. 3950-3962, 2021.
- [27] X. Zha, Y. Liu, and M. Huang, "Resilient Power Converter: A Grid-Connected Converter With Disturbance/Attack Resiliency via Multi-Timescale Current Limiting Scheme," *IEEE Journal on Emerging and Selected Topics in Circuits and Systems*, vol. 11, no. 1, pp. 59-68, 2021, doi: 10.1109/JETCAS.2021.3052252.
- [28] M. F. Umar, M. Hosseinzadehtaher, and M. B. Shadmand, "Enforcing Coherency in the Cluster of Grid-forming Inverters in Power Electronics-Dominated Grid," in 2021 IEEE 22nd Workshop on Control and Modelling of Power Electronics (COMPEL), 2021: IEEE, pp. 1-7.



- [29] M. F. Umar, M. Hosseinzadehtaher, and M. B. Shadmand, "Homogeneity realization for cluster of heterogeneous grid-forming inverters," in 2021 6th IEEE Workshop on the Electronic Grid (eGRID), 2021: IEEE, pp. 01-06.
- [30] M. F. Umar, M. Hosseinzadehtaher, and M. B. Shadmand, "Enabling Aggregation of Heterogenous Grid-Forming Inverters via Enclaved Homogenization," *IEEE access*, vol. 10, pp. 94765-94777, 2022.
- [31] A. Gohari, M. F. Umar, and M. B. Shadmand, "Coherency-based Coordination Scheme to Mitigate Adverse Dynamic Interaction of Grid-Forming Inverters," in 2023 IEEE Energy Conversion Congress and Exposition (ECCE), 2023: IEEE, pp. 1089-1095.
- [32] M. F. Umar, M. Hosseinzadehtaher, M. B. Shadmand, H. Livani, and M. Ben-Idris, "A Corrective Scheme to Prevent Adverse Dynamic Interaction of Grid-forming Inverters," in 2023 IEEE Power & Energy Society Innovative Smart Grid Technologies Conference (ISGT), 2023: IEEE, pp. 1-5.
- [33] M. F. Umar, A. G. Nazari, and M. B. Shadmand, "Coherency Enforcement in the Cluster of Heterogeneous Grid-forming and Gridfollowing Inverters," in 2023 IEEE Energy Conversion Congress and Exposition (ECCE), 2023: IEEE, pp. 1110-1115.
- [34] S. D'Arco and J. A. Suul, "Equivalence of virtual synchronous machines and frequency-droops for converter-based microgrids," *IEEE Transactions on Smart Grid*, vol. 5, no. 1, pp. 394-395, 2013.
- [35] H. A. Young, V. A. Marin, C. Pesce, and J. Rodriguez, "Simple finite-control-set model predictive control of grid-forming inverters with LCL filters," *IEEE Access*, vol. 8, pp. 81246-81256, 2020.



Muhammad F. Umar (M'23) received his B.Sc. degree in Electrical engineering from Lahore University of Management Sciences, Pakistan, in 2014. He has done master's in electrical Power Engineering from U.S. Pakistan Center for Advanced Studies in Energy, National University of Sciences and Technology, Pakistan in 2018. He did his Ph.D. degree in Electrical and Computer

Engineering Department at University of Illinois at Chicago, USA in 2023. He was 2019 Fulbright Fellowship Awardee. Currently, he is a postdoctoral research associate at Texas A&M University at Qatar, Doha, Qatar.



Amirhosein Gohari (student member, IEEE) received his B.Sc. and M.Sc. in electrical engineering and power electronics from Shahid Beheshti University, Tehran, Iran in 2015 and 2018 respectively, both with "first-rank student" honor. From 2018, he was a research assistant with the faculty of electrical engineering at Shahid Beheshti University. During his career, he acquired

valuable experience in designing and implementing power electronics converters. His research interests include power electronics, multilevel inverters, and soft switching. Since Fall 2022, he is pursuing a Ph.D. degree in the Department of Electrical and Computer Engineering at the University of Illinois at Chicago (UIC).



Mohammad B. Shadmand (M'15-SM'20) received the Ph.D. degree in electrical engineering from Texas A&M University, College Station, TX, USA, in 2015. From 2017 to 2020, he was an Assistant Professor with the Department of Electrical and Computer Engineering, Kansas State University, Manhattan, KS, USA. Since 2020, he is an Associate Professor with the

University of Illinois at Chicago, IL, USA. Dr. Shadmand was awarded Michelle Munson Serban Simu Keystone Research Scholar, Kansas State University in 2017. He was awarded the 2019 IEEE Myron Zucker Faculty-Student Research Grant. He has awarded multiple best paper awards at different IEEE conferences. He is the General Co-Chair of 50th Annual Conference of the IEEE Industrial Electronics Society (IECON 2024), Chicago, IL. He serves as Associate Editor of IEEE Transactions on Industrial Electronics and IET Renewable Power Generation.



Haitham Abu-Rub (Fellow, IEEE) is a professor at Hamad bin Khalifa University. He received two PhDs, one in electrical engineering from the Gdansk University of Technology, Poland, in 1995, and the second Ph.D. degree in humanities from Gdansk University, Poland, in 2004.

Abu-Rub has research and teaching experiences at many universities in many

countries including Qatar, Poland, Palestine, USA, and Germany. He has served for five years as the chair of Electrical and Computer Engineering Program at Texas A&M University at Qatar and for ten years as the managing director of the Smart Grid Center at the same university.

Abu-Rub is the recipient of many national and international awards and recognitions. He is the recipient of Fulbright and Alexander von Humboldt scholarships. His research group includes many PhD students and postdoctoral fellows.

Abu-Rub has published over 600 journal and conference papers, three patents, eight books, and eight book chapters. He has offered numerous keynote speeches at many conferences, training courses for industry engineers, and special courses for students.

Abu-Rub is a Fellow of IEEE and Co-Editor in Chief of the IEEE Transactions on Industrial Electronics.